Strain-Rate-Dependent Mechanical Behavior of a Non-Equimolar CoCrFeMnNi High Entropy Alloy with a Segmented Coarse Grain Structure

Haoyang Li[a,*], Chenwei Shao[b], Okan K. Orhan[c], David Funes Rojas[c], Mauricio Ponga[c,**], James D. Hogan[a]

[a] *Department of Mechanical Engineering, University of Alberta, Edmonton, AB T6G 2R3, Canada*
[b] *Laboratory of Fatigue and Fracture for Materials, Institute of Metal Research, Chinese Academy of Sciences, Shenyang 110016, People's Republic of China*
[c] *Department of Mechanical Engineering, University of British Columbia Vancouver Campus, BC V6T 1Z4, Canada*

Abstract

The mechanical response of a $Co_{11.3}Cr_{20.4}Fe_{22.6}Mn_{21.8}Ni_{23.9}$ (wt%) high entropy alloy with a segmented coarse grain structure is investigated using strain-rate-dependent uniaxial compression experiments. The composition is verified using ab-initio simulations by examining thermal stability through the reduction of Gibbs free energy relative to similar equi-molar alloys. The segmented grain structure, combining high-angle coarse-grains with low-angle sub-grains, provides good hardness ($\sim$ 3 GPa) and strain-hardening ($\sim$ 2600 MPa/ε). Yield strength shows strain-rate-dependent behavior with high strain-rate sensitivity. Here, the macroscopic deformation is correlated with the microscopic plastic failure mechanisms, facilitated by advanced in situ visualization and analysis. Results reveal that the formation of deformation bands occur before yield, while the interactions between microscopic plastic deformation mechanisms and the low-angle sub-grain boundaries significantly affect the apparent surface deformation features and mechanical properties.

Keywords: high entropy alloy, compression testing, strain-rate sensitivity,

*Corresponding author
**Corresponding author
Email addresses: haoyang@ualberta.ca (Haoyang Li), mponga@mech.ubc.ca (Mauricio Ponga)

low-angle sub-grain structure, electron backscatter diffraction (EBSD)

1. Introduction

High-entropy alloys (HEA) are developed to replace some conventional alloys (e.g., Co- and Ni-based superalloys) because of the possibility to attain improved mechanical performance (e.g., thermal stability, strength/hardness-ductility trade-off) [1–3]. The combination of multiple principal elements in relatively high concentrations expands the metallic alloying space [4, 5], and therefore, allows property tailoring for specific applications (e.g., aerospace [6, 7] and nuclear [8, 9]). Furthermore, the high mixing entropy between atoms reduces the chance of intermetallic phases and usually forms random solid solutions, which enhances microstructural and mechanical stabilities and promotes solid solution strengthening [10–14]. Among the large element space, the CoCrFeMnNi (known as "Cantor") alloy [15] has been well studied in the literature because of its ease of manufacturing and the resulting single solid solution as face-centered cubic (FCC) below its solidus temperature [16–18]. To date, varying properties and deformation mechanisms of CoCrFeMnNi alloys have been noted depending on element content and grain structure [19]. In the literature, studies have also been conducted on variations of CoCrFeMnNi alloys in order to probe the dynamic mechanical response under compressive loading [20–29]. For example, Li et al. [20] studied the adiabatic shear localization in an equiatomic CoCrFeMnNi alloy under dynamic shear compression and found a high shear strain threshold ($\sim 7\%$) for the initiation of adiabatic shear bands. The high resistance to shear banding was attributed to the excellent strain-hardening ability competing with only moderate thermal softening [20]. In another dynamic failure study on a single FCC CoCrFeMnNi alloy [23], electron backscatter diffraction (EBSD) analysis showed strong localized deformation regions, and thermal softening was observed from the strain-hardening evolution curves.

In the current study, we investigate mechanical properties and failure of a $Co_{11.3}Cr_{20.4}Fe_{22.6}Mn_{21.8}Ni_{23.9}$ (wt%) high entropy alloy with segmented coarse

grained structures (SCG-HEA) using uniaxial compression experiments at different strain rates. We specifically focus on an alloy with a lower Co content to explore the effect of non-equimolar mixing on the mechanical response, while: (i) it can still retain full solubility with single FCC phase [15]; and (ii) it can at least have comparable and potentially improved mechanical properties when compared to other Cantor-like equiatomic HEAs [21]. Lowering the content of the heavy element (i.e., Co) could also potentially reduce the vibrational Helmholtz free energy at the expense of lower configurational entropy, which leads to further reduction in Gibbs free energy [30]. For the first time in the literature on CoCrFeMnNi alloys, this study yields new discoveries on the relationships between microstructure and macroscale deformation mechanisms, facilitated by the use of *state-of-the-art* in situ visualizations.

2. Materials and Methods

Ingots with a composition of $Co_{11.3}Cr_{20.4}Fe_{22.6}Mn_{21.8}Ni_{23.9}$ (wt%) were received from Eutectix LLC (Chatham, NJ, USA). Five pure metal powders Co, Cr, Fe, Mn, and Ni were pre-mixed and inductive vacuum melted (IVM) before cast into cylinders with diameters of $\sim$ 8.5 cm and heights of $\sim$ 3.5 cm (ρ = 7.72 $\pm$ 0.08 g/cm^3). The composition of the material (see Supplementary Table 1) was confirmed using the inductively coupled plasma mass spectrometry (ICP-MS), energy dispersive spectroscopy (EDS), and X-ray photoelectron spectroscopy (XPS) methods. The phase of the SCG-HEA was identified using X-ray diffraction (XRD) with CuKα radiation. Scanning electron microscope (SEM) equipped with EDS and electron backscatter diffraction detector (EBSD) was used to investigate the microstructural features and deformation mechanisms. Cubic samples with nominal dimensions of 3.5 $\times$ 4.0 $\times$ 5.0 mm^3 were electrical discharge machined (EDM), mechanically polished to less than 0.1 μm, and electro-chemically etched for EBSD analysis. Room temperature strain-rate-dependent uniaxial compression experiments were performed using the cubic samples with loading direction parallel to the 5.0 mm edge. Quasi-

static experiments were conducted using a servo-hydraulic MTS 810 machine on displacement control. Dynamic experiments were carried out on a modified split-Hopkinson pressure bar (SHPB) setup [31], with details found in [32]. High-speed cameras (Shimadzu HPV-X2 and PROMON U750) were used in all experiments to capture surface deformation and use for 2D-Digital Image Correlation (2D-DIC) analysis. All strain information was acquired by DIC and matched in time with the stress histories to yield stress-strain curves. The Vickers hardness was measured using a Wilson VH1102 micro-hardness tester with a 200 g load applied over a dwell time of 15 seconds. Results were averaged over 15 valid measurements.

3. Results and Discussion

First, the composition selection of the current SCG-HEA is verified using ab-initio simulations by computing the temperature-dependent relative Gibbs free energy (ΔG) for both Co-reduced (i.e., $Co_{0.1}$) and Co-rich (i.e., $Co_{0.3}$) cases with respect to the equimolar CoCrFeMnNi alloy (see Figure 1). For computational details, please refer to Appendix A in the Supplementary Document. In Figure 1, the ΔG of $Co_{0.1}(CrFeMnNi)_{0.9}$ show a subtle increment up to $\sim$ 100 K after which it decreases monotonically with increasing temperature. For $Co_{0.3}(CrFeMnNi)_{0.7}$, the ΔG increased monotonically with increasing temperature. In addition, it is evident that the vibrational Helmholtz energy differences (ΔF_{vib}) is the dominant factor for compensating the loss in configurational entropy and, therefore, achieving the relative thermal stability (see Supplementary Figure 1). The overall reduction in the Gibbs free energy show that the current SCG-HEA with a low percentage of Co is thermally more stable than similar CoCrFeMnNi alloys fabricated with equimolar or Co-rich composition, demonstrating a better consistency in achieving desired end products.

Stemming from the thermally more stable composition, a single solid solution with face centered cubic (FCC) structure for the SCG-HEA is identified from the 1D-XRD spectrum (see Supplementary Figure 2) [15]. The EBSD in-

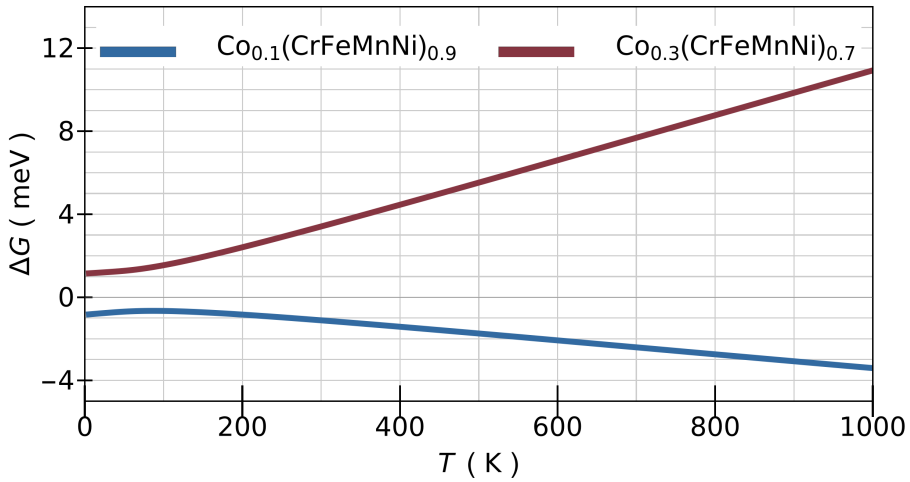

Figure 1: Temperature-dependent relative Gibbs free energy (ΔG) of the Co-reduced $Co_{0.1}(CrFeMnNi)_{0.9}$ and Co-rich $Co_{0.3}(CrFeMnNi)_{0.7}$ alloys with respect to the equimolar CoCrFeMnNi alloys.

verse pole figure (IPF) maps in Figure 2 shows a segmented grain structure in the current SCG-HEA, whereas a high-angle coarse grain (HACG) boundary is identified in Figure 2a and numerous low-angle sub-grain (LASG) boundaries (with mis-orientation $< 15°$ [33]) are observed in Figure 2b. The definition of sample orientation and the standard IPF indexing triangle are demonstrated in Figure 2c and d, respectively. Specifically, in Figure 2a, the two coarse grains (yellow and blue) with grain sizes > 600 μm are observed (boundary outlined by black-solid-lines). It is observed from the reduced IPF triangle in Figure 2a that the distribution of the two HACGs is concentrated in two specific regions, indicating a large mis-orientation between the two grains. Minor changes in orientation (shown as deep orange color in the IPF map) are observed on the yellow grain, and these are identified as the LASG boundaries (outlined by black-dotted-lines). Figure 2b shows the LASGs on a single HACG at a larger scale. The reduced IPF triangle confirms the existence of a single coarse grain with a crystalline orientation of (001). The LASG boundaries are shown as band-like mis-orientations with yellow or light purple colours. Lastly, limited

processing-induced plastic deformation is observed, and this is expected since the material has not undergone rolling nor annealing.

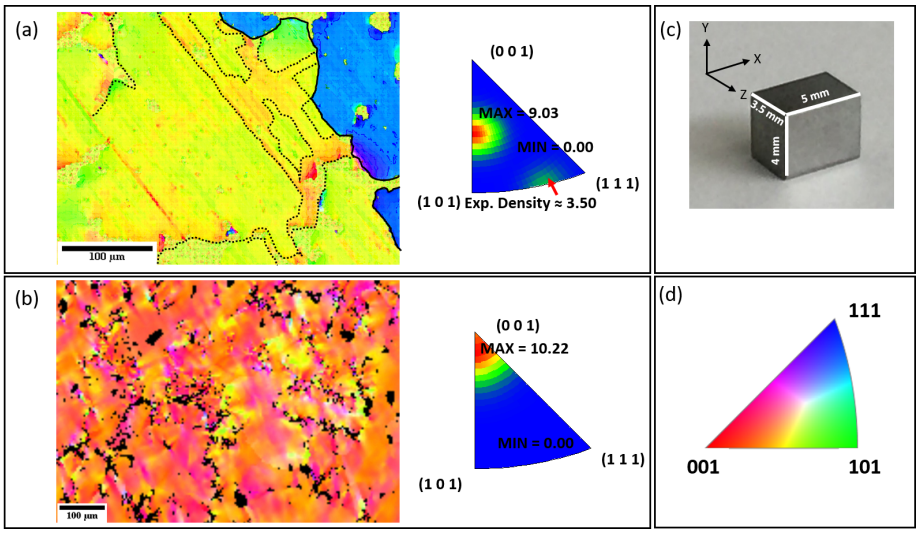

Figure 2: EBSD IPF maps showing a segmented grain structure in the SCG-HEA with (a) high-angle coarse grains (HACGs) and (b) low-angle sub-grains (LASGs) within a coarse grain. The LASG boundaries are shown as the slight colour changes. We outline a portion of HACG (black-solid-lines) and LASG (black-dotted-lines) boundaries in (a) as an example. The reduced IPF triangles show concentrated regions for grain distribution, with the orientations of the HACGs at maximum experimental densities (Exp. Density) ≈ 10. (c) the definition of sample orientation. (d) the standard IPF indexing triangle.

Next, we further investigate the LASG boundaries on a single HACG using EDS in Figure 3. The characteristic elemental X-ray energy peaks in Figure 3a confirms the existence of only the five elements (Cr, Co, Fe, Mn, Ni) in the SCG-HEA, with high concentrations of Mn and Ni and low concentrations of Co, Cr, and Fe observed in the underlying thick bands (Figure 3b with bands encompassed by red-dashed-lines). Investigations at other locations confirm this observation (see Supplementary Figure 3). The width of these thick bands has an average of 11.3 ± 2.4 μm, and this is consistent with the measurements taken using the EBSD maps in Figure 2. These Ni, Mn-concentrated bands located at the LASG boundaries segment the seemingly coarse grain into smaller regions.

The formation of LASGs and differences in elemental concentrations at the sub-grain boundaries are likely the combined consequence of the low content of Co (~ 10 wt%) and processing conditions [34–36]. Past studies have been conducted to explore the influence of LASGs on the mechanical performance of metallic alloys and HEAs (e.g., Mg-alloys [37], steels [38], Ti-alloys [39], and various HEAs [40–44]), where positive effects on mechanical properties were observed (e.g., strength, ductility).

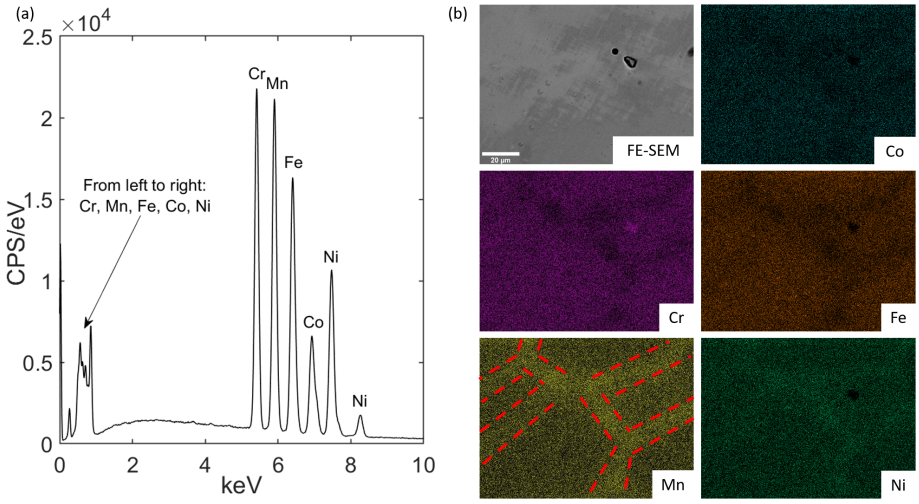

Figure 3: Elemental distribution and composition are investigated using EDS, where (a) shows the characteristic peaks for all five elements (i.e., Co, Cr, Fe, Mn, Ni). (b) outlines of the underlying thick band features (highlighted by red-dashed-lines) are observed with high concentrations of Mn and Ni and low concentrations of Co, Cr, and Fe elements. These bands constituting the LASG boundaries generate a segmentation of the seemingly coarse grain.

Figure 4 summarizes the mechanical properties of the SCG-HEA (see Supplementary Table 2 for summary). The strain-rate-dependent engineering compressive stress-strain curves in Figure 4a demonstrates representative behavior from $\sim 10^{-4}$ to $\sim 2 \times 10^{3}$ s^{-1}. In general, a short linear-elastic region (to $\sim$ 0.001 strain) is observed. The gradient of the linear region with an average of 96.2 ± 4.1 GPa is defined as the Young's modulus of the SCG-HEA. The Poisson's ratio, determined by averaging the slopes of the quasi-static lateral *vs.*

axial strain curves taken at 0.001 strain, is found to be 0.350 ± 0.026. Continuous strain-hardening at a steadily lower rate occurs after yield, with no distinct changes in the hardening rate at large strains. In this case, we truncate the curves at 6% strain to compensate for experiments which the DIC correlation is lost because surface deformation, as well as to preserve the 2D-DIC in-plane deformation assumption. An virtual extensometer is applied to verify the overall strain computed by the DIC method. The right-arrow indicates a continuation of the stress-strain curves. In all experiments, the SCG-HEA does not fracture at the maximum tested strain up to ~ 0.21, with an apparent ultimate compressive strength ~ 850 MPa under dynamic loading (obtained from the stress histories).

Next, the engineering yield strength (extracted using the 0.002 offset method) is plotted against the strain rate from $\sim 10^{-4}$ to $\sim 2 \times 10^{3}$ s^{-1} in a semi-logarithmic scale in Figure 4b, following the Lindholm approach [45, 46]:

$$\sigma = \sigma_0 + m_L \log(\dot{\varepsilon}) \tag{1}$$

where σ_0 is the lower-end of the yield strength and m_L is known as the Lindholm strain-rate sensitivity. The Lindholm approach was proposed to represent the strain-rate sensitivity of metals under SHPB testing [46], and it uses a single-$\log_{10}$ strain rate scaling compared to the double-natural logarithmic approach commonly used in some other literature [47, 48]. This method generates a more sensitive change in m_L, while preserving the true values and the trend of the corresponding property.

Three piece-wise functions in the form of Equation (1) are fitted to the dataset corresponding to the quasi-static, dynamic upper bound, and dynamic lower bound, respectively. The SCG-HEA exhibits a gradual increase in yield strength in the quasi-static regime from ~ 150 MPa at $\sim 10^{-4}$ s^{-1} to ~ 180 MPa at ~ 0.67 s^{-1}, with a m_L of 3.2. A transition appears to occur at ~ 1 s^{-1} (often denoted as the characteristic strain rate [49]), where the yield strength increases much faster with respect to the strain rate. We propose an upper bound and a lower bound to encompass the scattered data points, with the m_L being 37.7 and 12.6,

respectively. It is observed that the majority of the data-points cluster around the upper bound with an increase from $\sim$ 180 MPa at $\sim$ 0.67 s^{-1} to $\sim$ 340 MPa at $\sim$ 2200 s^{-1}. An outlier at $\sim$ 120 s^{-1} (red-dashed-line circled) is omitted from the fitted data-set. The true reason of this abnormal behavior needs to be investigated further, and it could be an effect of the superposition between grain orientation and the macroscopic deformation bands (see Supplementary Figure 4). Overall, the strain-rate sensitivity of the SCG-HEA is similar to the ones reported in other CoCrFeMnNi alloys in the literature [21, 23, 25, 28], but the LASG structure does not seem to have an effect on the absolute values of the yield strength [40].

Next, Figure 4c demonstrates that the strain-hardening rate of the SCG-HEA reaches $\sim$ 2600 MPa/ε at all strain rates. With a similar coarse grain size, the current SCG-HEA has a much higher strain-hardening rate than a previously studied $Al_{0.3}$CoCrFeNi alloy ($\sim$ 1200 MPa/ε) [50] and a cast CoCrFeMnNi alloy ($\sim$ 600 MPa/ε) [42]. This is likely attributed to the LASG boundaries, which allow a higher areal density of dislocations and slip bands for further hardening to occur [41, 51]. Lastly, significant improvement in micro-hardness is promoted by the LASG structure (see Figure 4d). Measurements of the SCG-HEA hardness (red-dashed-line circled, 2.84 $\pm$ 0.09 GPa (X-Y) and 3.13 $\pm$ 0.13 GPa (Y-Z)) are $>$ 2.5x higher than other CoCrFeMnNi alloys from the literature with similar coarse grain sizes [52, 53]. In addition, according to the bounded region by two widely-adapted Hall-Petch hardness relations for CoCrFeMnNi alloys [54, 55], the SCG-HEA has a micro-hardness equivalent to an effective grain size between 1 and 10 μm. Huang et al. [56] investigated the role of low-angle grain boundaries on the micro-hardness of aluminum and concluded that the low-angle boundaries could contribute to strengthening similar to high-angle grain boundaries.

Next, we examine the characteristics of macroscopic surface deformation using images from the high-speed camera (see Figure 5, examples of high-speed videos provided in supplementary files). Figure 5a (strain rate of $\sim$ 0.0005 s^{-1}) and Figure 5b (strain rate of $\sim$ 2000 s^{-1}) without the speckle patterns show the

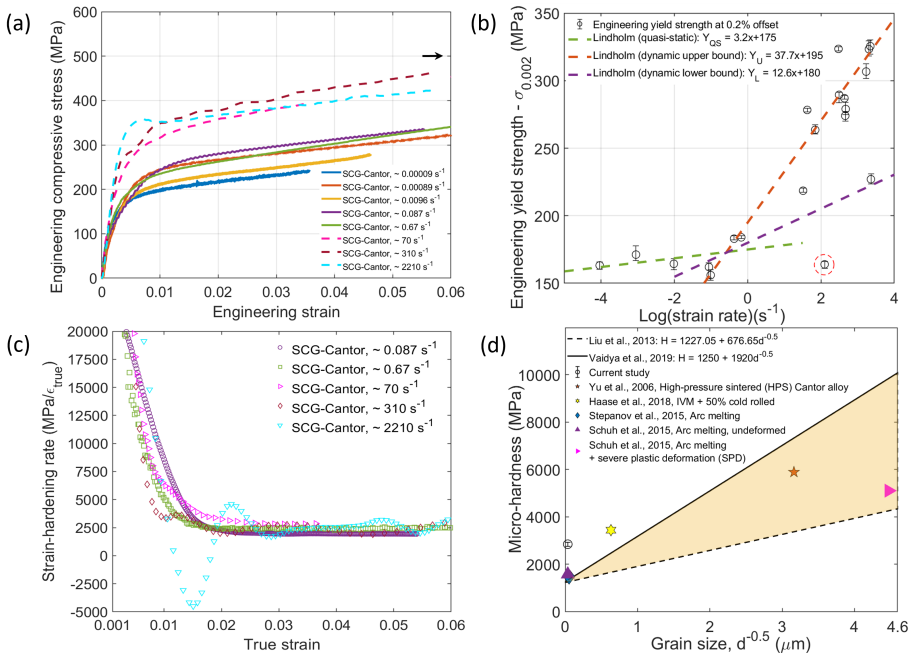

Figure 4: Summary of mechanical properties. (a) engineering stress-strain curves from $\sim 10^{-4}$ to $\sim$ 2 x 10^3 s^{-1}. Note that the curves do not show the later part of the stress-strain behavior because of the correlation loss in DIC at large deformation. The right-arrow indicates the continuation of the curves. (b) engineering yield strength at different strain rates with piece-wise Lindholm fit [46] for rate sensitivity. Red-dashed-circle highlights an outlier data point. (c) strain-hardening rate at different strain rates, with colors matched with their corresponding stress-strain curves in (a). (d) micro-hardness measurements with Hall-Petch bounds. Red-dashed-circle highlights the data from the current study.

initiation and propagation of global deformation up to 0.05 strain. In both cases, we observe the formation of localized bands at $\sim$ 0.001 strain (red arrows), which correlates well with the end of the linear-elastic region in the stress-strain curves (see Figure 4a). These bands grow in both size and quantity with increasing strains (red lines), and finally result in the appearance of secondary localized deformation features. In all experiments, we observed band formation at small strains but dissimilar macroscopic deformation patterns at large strains. For example, the quasi-static experiment (see Figure 5a) shows the emergence of a bulky region with more bands growing inside the region at $\sim$ 0.02 strain, while

the dynamic experiment (see Figure 5b) reveals only band bifurcations. The initiation of the deformation bands at low strains could be related to the slip bands interacting with LASG structures [57], while the difference in secondary deformation at high strains may stem from the HACGs with slip bands confined to the grain boundary [58]. In Figure 5c (strain rate of $\sim 0.67\ s^{-1}$) and Figure 5d (strain rate of $\sim 300\ s^{-1}$), we superimpose the DIC axial strain contours on the high-speed images to investigate the band formation before yield (up until $\varepsilon \sim 0.005$). We verify the start of band formation at ~ 0.001 strain, where localized axial strain zones start to form (i.e., left edge in Figure 5c and right edge in Figure 5d). Further accumulation of localized axial strains result in a final strain of ~ 0.01 in the band regions even though the global strain is only half of that value.

Finally, *post-mortem* interactions between slip bands, deformation bands, and grain structures of the SCG-HEA are investigated using EBSD (Figure 6). These deformation mechanisms are common at all strain rates: (a) and (b) for $\sim 0.0001\ s^{-1}$, (c) and (d) for $\sim 0.67\ s^{-1}$, and (e) and (f) for $\sim 2300\ s^{-1}$. It is observed in the band contrast maps that ordinary slip bands (darker lines) tend to aggregate in the vicinity of HACG boundaries without crossing-over (see Figure 6a, c, and e). In the IPF maps, it is evident that these slip bands appear everywhere in the microstructures with slight color differences to the surrounding materials, indicating slip being the dominant deformation mechanism. The deformation bands (encompassed by black-dashed-lines) in Figure 6b, d, and f have an average of $226 \pm 57\ \mu$m in width, with cross-slips growing perpendicular to the band boundaries. This correlates well with the observations made in the high-speed images (Figure 5).

Additional LASG growth is shown as blue sharp bands in Figure 6d, and these appear under all loading conditions. A point-to-point mis-orientation map is used to confirm the LASG growth (see Figure 6g), where the blue bar chart indicates that the mis-orientation is mostly less than 10°. The growth of LASGs could be caused by the misalignment between loading direction and sub-grain boundaries [59, 60]. It is also observed that both ordinary slip bands and cross-

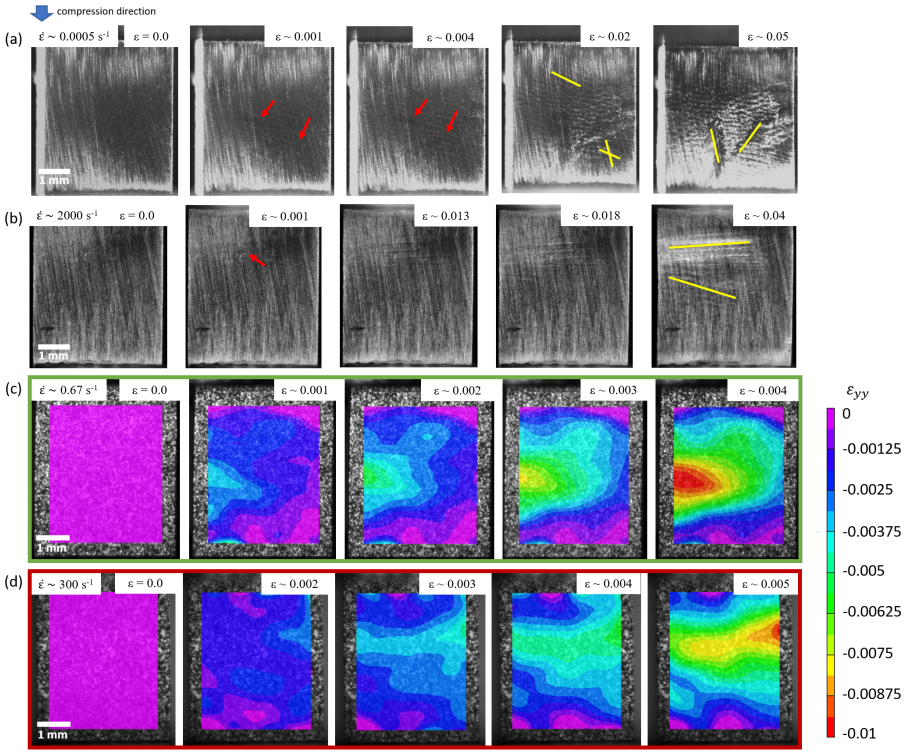

Figure 5: High-speed images showing macroscopic deformation bands and their interactions at different strains and strain rates. (a) and (b) without speckle pattern showing global deformation evolution up to $\sim$ 0.05 strain. Red arrows indicate the initiation of deformation bands, and yellow lines outline the deformation band growth and secondary localized deformation regions. (c) and (d) with DIC contours showing local strain accumulation near the yield strain.

slips do not stop at LASG boundaries (see Figure 6c and d), and this is likely due to the overall lower stacking fault energy of the LASGs, which is better at improving ductility [61]. We propose that the LASG structure reduces the effective grain size of the SCG-HEA and promotes grain boundary strengthening [51], and therefore, enhances the mechanical properties (see Figure 4) and affects the deformation mechanisms (see Figure 6). Lastly, a plausible twin (see red arrow in Figure 6f) with the mis-orientation map showing $\sim 60°$ in difference with the surrounding material [62, 63]. We conclude that twinning is not a

dominant deformation mechanism across the strain rates and final strains that were investigated, but it could occur if higher loading rates are achieved [28].

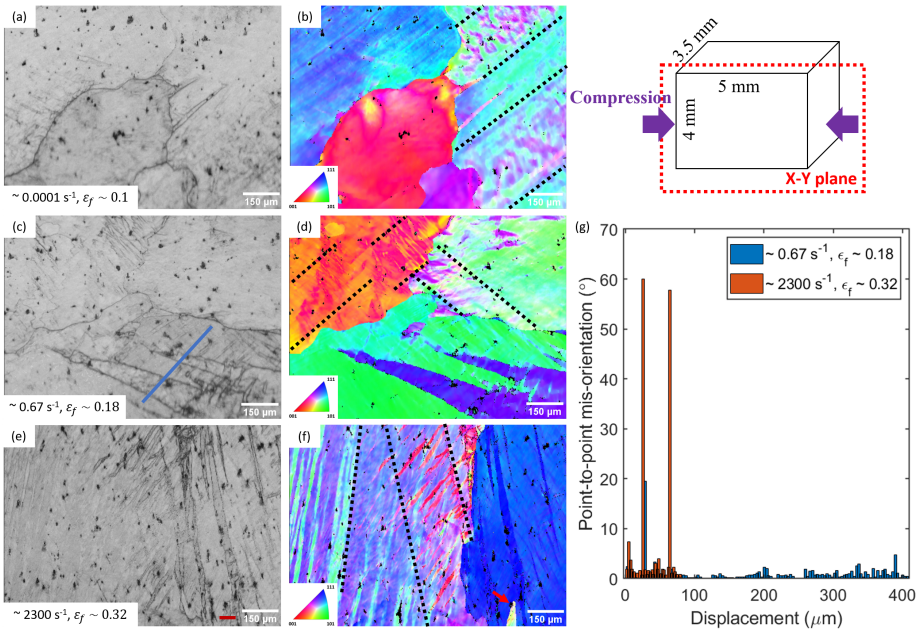

Figure 6: EBSD band contrast and IPF maps showing deformation bands (black-dashed-lines), slip bands (needles with differences in contrast with the surrounding materials), and cross slips (in between the black-dashed-lines) at different strain rates and final strains with: (a – b) ~ 0.0001 s^{-1} and ~ 0.1 strain, (c – d) ~ 0.67 s^{-1} and ~ 0.18 strain, and (e – f) ~ 2300 s^{-1} at ~ 0.32 strain. (g) mis-orientation mapping is used to investigate the sub-grain growth and potential twinning mechanisms. The blue line in (c) and the red line in (e) correspond to the analyzed regions which are shown as the same colour in (g).

4. Conclusion

In summary, this work unraveled the mechanical properties and deformation mechanisms of a non-equimolar $Co_{11.3}Cr_{20.4}Fe_{22.6}Mn_{21.8}Ni_{23.9}$ (wt%) high entropy alloy with a segmented coarse grain structure. The significantly reduced Gibbs free energy of this alloy composition shows better thermal stability than similar equimolar alloys. The material showed good micro-hardness and strain-hardening rate likely benefited from the LASG structure. High-speed imaging

coupled with DIC confirmed the initiation of deformation bands before yield, and this is critical in understanding pre-yield hardening behavior where this information is inaccessible without advanced in situ visualization and analysis. EBSD analysis examined the interplay among deformation bands, slips, and grain structures, where additional sub-grain growth allows further aggregation of slips and dislocations aiding in further strain-hardening. This study also explores a potential non-equimolar fabrication route for producing more affordable and sustainable materials while preserving the desired properties of other similar HEAs.

5. Acknowledgement

This work was supported by the Canadian IDEaS program under contract W7714-217552/001/ and NSERC Discovery Grant 2016-04685 (UAlberta) and 2016-06114 (UBC).

6. Data Availability

The raw/processed data related to this study can be shared per request to the corresponding author (Haoyang Li) at haoyang@ualberta.ca.

References

[1] J. Chen, X. Zhou, W. Wang, B. Liu, Y. Lv, W. Yang, D. Xu, Y. Liu, A review on fundamental of high entropy alloys with promising high–temperature properties, Journal of Alloys and Compounds 760 (2018) 15–30.

[2] W. Zhang, P. K. Liaw, Y. Zhang, Science and technology in high-entropy alloys, Science China Materials 61 (1) (2018) 2–22.

[3] M. C. Gao, J.-W. Yeh, P. K. Liaw, Y. Zhang, et al., High-entropy alloys, Cham: Springer International Publishing (2016).

[4] J.-W. Yeh, S.-K. Chen, S.-J. Lin, J.-Y. Gan, T.-S. Chin, T.-T. Shun, C.-H. Tsau, S.-Y. Chang, Nanostructured high-entropy alloys with multiple principal elements: novel alloy design concepts and outcomes, Advanced Engineering Materials 6 (5) (2004) 299–303.

[5] E. P. George, D. Raabe, R. O. Ritchie, High-entropy alloys, Nature Reviews Materials 4 (8) (2019) 515–534.

[6] M. Dada, P. Popoola, S. Adeosun, N. R. Mathe, High entropy alloys for aerospace applications, IntechOpen, 2019.

[7] A. E. Afolabi, A. P. I. Popoola, O. M. Popoola, High entropy alloys: Advance material for landing gear aerospace applications, Handbook of Nanomaterials and Nanocomposites for Energy and Environmental Applications (2020) 1–27.

[8] P. Barron, A. Carruthers, J. Fellowes, N. Jones, H. Dawson, E. Pickering, Towards v-based high-entropy alloys for nuclear fusion applications, Scripta Materialia 176 (2020) 12–16.

[9] E. J. Pickering, A. W. Carruthers, P. J. Barron, S. C. Middleburgh, D. E. Armstrong, A. S. Gandy, High-entropy alloys for advanced nuclear applications, Entropy 23 (1) (2021) 98.

[10] C.-Y. Cheng, Y.-C. Yang, Y.-Z. Zhong, Y.-Y. Chen, T. Hsu, J.-W. Yeh, Physical metallurgy of concentrated solid solutions from low-entropy to high-entropy alloys, Current Opinion in Solid State and Materials Science 21 (6) (2017) 299–311.

[11] A. Manzoor, S. Pandey, D. Chakraborty, S. R. Phillpot, D. S. Aidhy, Entropy contributions to phase stability in binary random solid solutions, npj Computational Materials 4 (1) (2018) 1–10.

[12] C. R. LaRosa, M. Shih, C. Varvenne, M. Ghazisaeidi, Solid solution strengthening theories of high-entropy alloys, Materials Characterization 151 (2019) 310–317.

[13] Y. P. Wang, B. S. Li, H. Z. Fu, Solid solution or intermetallics in a high-entropy alloy, Advanced engineering materials 11 (8) (2009) 641–644.

[14] F. Otto, Y. Yang, H. Bei, E. P. George, Relative effects of enthalpy and entropy on the phase stability of equiatomic high-entropy alloys, Acta Materialia 61 (7) (2013) 2628–2638.

[15] B. Cantor, Multicomponent and high entropy alloys, Entropy 16 (9) (2014) 4749–4768.

[16] K.-Y. Tsai, M.-H. Tsai, J.-W. Yeh, Sluggish diffusion in co–cr–fe–mn–ni high-entropy alloys, Acta Materialia 61 (13) (2013) 4887–4897.

[17] D. Ma, M. Yao, K. G. Pradeep, C. C. Tasan, H. Springer, D. Raabe, Phase stability of non-equiatomic cocrfemnni high entropy alloys, Acta Materialia 98 (2015) 288–296.

[18] M. Yao, K. G. Pradeep, C. C. Tasan, D. Raabe, A novel, single phase, non-equiatomic femnnicocr high-entropy alloy with exceptional phase stability and tensile ductility, Scripta Materialia 72 (2014) 5–8.

[19] E. P. George, W. Curtin, C. C. Tasan, High entropy alloys: A focused review of mechanical properties and deformation mechanisms, Acta Materialia 188 (2020) 435–474.

[20] Z. Li, S. Zhao, S. M. Alotaibi, Y. Liu, B. Wang, M. A. Meyers, Adiabatic shear localization in the crmnfeconi high-entropy alloy, Acta Materialia 151 (2018) 424–431.

[21] B. Wang, A. Fu, X. Huang, B. Liu, Y. Liu, Z. Li, X. Zan, Mechanical properties and microstructure of the cocrfemnni high entropy alloy under high strain rate compression, Journal of Materials Engineering and Performance 25 (7) (2016) 2985–2992.

[22] G. Soares, M. Patnamsetty, P. Peura, M. Hokka, Effects of adiabatic heating and strain rate on the dynamic response of a cocrfemnni high-entropy alloy, Journal of Dynamic Behavior of Materials 5 (3) (2019) 320–330.

[23] J. M. Park, J. Moon, J. W. Bae, M. J. Jang, J. Park, S. Lee, H. S. Kim, Strain rate effects of dynamic compressive deformation on mechanical properties and microstructure of cocrfemnni high-entropy alloy, Materials Science and Engineering: A 719 (2018) 155–163.

[24] Y. Qi, M. Zhao, M. Feng, Molecular simulation of microstructure evolution and plastic deformation of nanocrystalline cocrfemnni high-entropy alloy under tension and compression, Journal of Alloys and Compounds 851 (2021) 156923.

[25] B. Wang, X. Huang, A. Fu, Y. Liu, B. Liu, Serration behavior and microstructure of high entropy alloy cocrfemnni prepared by powder metallurgy, Materials Science and Engineering: A 726 (2018) 37–44.

[26] E.-W. Huang, C.-M. Lin, J.-Y. Juang, Y.-J. Chang, Y.-W. Chang, C.-S. Wu, C.-W. Tsai, A.-C. Yeh, S. R. Shieh, C.-P. Wang, et al., Deviatoric deformation kinetics in high entropy alloy under hydrostatic compression, Journal of Alloys and Compounds 792 (2019) 116–121.

[27] A. V. Korchuganov, Onset of plastic deformation in non-equiatomic fcc cocrfemnni high-entropy alloys under high-speed loading, Letters on Materials 8 (3) (2018) 311–316.

[28] S.-P. Tsai, Y.-T. Tsai, Y.-W. Chen, P.-J. Chen, P.-H. Chiu, C.-Y. Chen, W.-S. Lee, J.-W. Yeh, J.-R. Yang, High-entropy cocrfemnni alloy subjected to high-strain-rate compressive deformation, Materials Characterization 147 (2019) 193–198.

[29] H. Jeong, H. Park, K. Park, T. Na, W. Kim, High-temperature deformation mechanisms and processing maps of equiatomic cocrfemnni high-entropy alloy, Materials Science and Engineering: A 756 (2019) 528–537.

[30] D. B. Miracle, O. N. Senkov, A critical review of high entropy alloys and related concepts, Acta Materialia 122 (2017) 448–511.

[31] W. W. Chen, B. Song, Split Hopkinson (Kolsky) bar: design, testing and applications, Springer Science & Business Media, 2010.

[32] C. Lo, H. Li, G. Toussaint, J. D. Hogan, On the evaluation of mechanical properties and ballistic performance of two variants of boron carbide, International Journal of Impact Engineering 152 (2021) 103846.

[33] M. Winning, A. D. Rollett, Transition between low and high angle grain boundaries, Acta materialia 53 (10) (2005) 2901–2907.

[34] C. Zhang, C. Zhu, S. Shin, K. Vecchio, Enhancement of¡ 001¿ recrystallization texture in non-equiatomic fe-ni-co-al-based high entropy alloys by combination of annealing and cr addition, Journal of Alloys and Compounds 768 (2018) 277–286.

[35] K. G. Pradeep, C. C. Tasan, M. Yao, Y. Deng, H. Springer, D. Raabe, Non-equiatomic high entropy alloys: Approach towards rapid alloy screening and property-oriented design, Materials Science and Engineering: A 648 (2015) 183–192.

[36] M. Mohammad-Ebrahimi, A. Zarei-Hanzaki, H. Abedi, S. Vakili, C. Soundararajan, The enhanced static recrystallization kinetics of a non-equiatomic high entropy alloy through the reverse transformation of strain

induced martensite, Journal of Alloys and Compounds 806 (2019) 1550–1563.

[37] H. Somekawa, D. A. Basha, A. Singh, Change in dominant deformation mechanism of mg alloy via grain boundary control, Materials Science and Engineering: A 746 (2019) 162–166.

[38] W. Wang, Y. Shan, K. Yang, Study of high strength pipeline steels with different microstructures, Materials Science and Engineering: A 502 (1-2) (2009) 38–44.

[39] S. Chen, Q. Yu, The role of low angle grain boundary in deformation of titanium and its size effect, Scripta Materialia 163 (2019) 148–151.

[40] S. Sun, Y. Tian, H. Lin, X. Dong, Y. Wang, Z. Zhang, Z. Zhang, Enhanced strength and ductility of bulk cocrfemnni high entropy alloy having fully recrystallized ultrafine-grained structure, Materials & Design 133 (2017) 122–127.

[41] W. Fang, R. Chang, X. Zhang, P. Ji, X. Wang, B. Liu, J. Li, X. He, X. Qu, F. Yin, Effects of cobalt on the structure and mechanical behavior of non-equal molar coxfe50- xcr25ni25 high entropy alloys, Materials Science and Engineering: A 723 (2018) 221–228.

[42] F. Xiong, R.-d. Fu, Y.-j. Li, D.-l. Sang, Effects of nitrogen alloying and friction stir processing on the microstructures and mechanical properties of cocrfemnni high-entropy alloys, Journal of Alloys and Compounds 822 (2020) 153512.

[43] S. S. Nene, K. Liu, M. Frank, R. S. Mishra, R. E. Brennan, K. C. Cho, Z. Li, D. Raabe, Enhanced strength and ductility in a friction stir processing engineered dual phase high entropy alloy, Scientific reports 7 (1) (2017) 1–7.

[44] J. J. Licavoli, M. C. Gao, J. S. Sears, P. D. Jablonski, J. A. Hawk, Microstructure and mechanical behavior of high-entropy alloys, Journal of Materials Engineering and Performance 24 (10) (2015) 3685–3698.

[45] X. Lin, D. Chen, Strain hardening and strain-rate sensitivity of an extruded magnesium alloy, Journal of materials engineering and performance 17 (6) (2008) 894–901.

[46] U. Lindholm, Some experiments with the split hopkinson pressure bar, Journal of the Mechanics and Physics of Solids 12 (5) (1964) 317–335.

[47] Y. Wang, E. Ma, Strain hardening, strain rate sensitivity, and ductility of nanostructured metals, Materials Science and Engineering: A 375 (2004) 46–52.

[48] Q. Wei, S. Cheng, K. Ramesh, E. Ma, Effect of nanocrystalline and ultrafine grain sizes on the strain rate sensitivity and activation volume: fcc versus bcc metals, Materials Science and Engineering: A 381 (1-2) (2004) 71–79.

[49] Y. Wang, A. Hamza, E. Ma, Temperature-dependent strain rate sensitivity and activation volume of nanocrystalline ni, Acta Materialia 54 (10) (2006) 2715–2726.

[50] Z. Li, S. Zhao, H. Diao, P. Liaw, M. Meyers, High-velocity deformation of al 0.3 cocrfeni high-entropy alloy: Remarkable resistance to shear failure, Scientific reports 7 (1) (2017) 1–8.

[51] B. Liu, D. Raabe, P. Eisenlohr, F. Roters, A. Arsenlis, G. Hommes, Dislocation interactions and low-angle grain boundary strengthening, Acta Materialia 59 (19) (2011) 7125–7134.

[52] B. Schuh, F. Mendez-Martin, B. Völker, E. P. George, H. Clemens, R. Pippan, A. Hohenwarter, Mechanical properties, microstructure and thermal stability of a nanocrystalline cocrfemnni high-entropy alloy after severe plastic deformation, Acta Materialia 96 (2015) 258–268.

[53] N. Stepanov, M. Tikhonovsky, N. Yurchenko, D. Zyabkin, M. Klimova, S. Zherebtsov, A. Efimov, G. Salishchev, Effect of cryo-deformation on structure and properties of cocrfenimn high-entropy alloy, Intermetallics 59 (2015) 8–17.

[54] M. Vaidya, A. Anupam, J. V. Bharadwaj, C. Srivastava, B. Murty, Grain growth kinetics in cocrfeni and cocrfemnni high entropy alloys processed by spark plasma sintering, Journal of Alloys and Compounds 791 (2019) 1114–1121.

[55] W. Liu, Y. Wu, J. He, T. Nieh, Z. Lu, Grain growth and the hall–petch relationship in a high-entropy fecrnicomn alloy, Scripta Materialia 68 (7) (2013) 526–529.

[56] F. Huang, N. Tao, Effects of strain rate and deformation temperature on microstructures and hardness in plastically deformed pure aluminum, Journal of Materials Science & Technology 27 (1) (2011) 1–7.

[57] P. Moretti, M.-C. Miguel, M. Zaiser, S. Zapperi, Depinning transition of dislocation assemblies: Pileups and low-angle grain boundaries, Physical Review B 69 (21) (2004) 214103.

[58] Z. Zhang, Z. Wang, J. Eckert, What types of grain boundaries can be passed through by persistent slip bands?, Journal of materials research 18 (5) (2003) 1031–1034.

[59] S. Xu, S. Kamado, N. Matsumoto, T. Honma, Y. Kojima, Recrystallization mechanism of as-cast az91 magnesium alloy during hot compressive deformation, Materials Science and Engineering: A 527 (1-2) (2009) 52–60.

[60] N. Y. Zolotorevsky, V. Rybin, A. Matvienko, E. Ushanova, S. Philippov, Misorientation angle distribution of deformation-induced boundaries provided by their ebsd-based separation from original grain boundaries: Case study of copper deformed by compression, Materials Characterization 147 (2019) 184–192.

[61] B. S. Murty, J.-W. Yeh, S. Ranganathan, P. Bhattacharjee, High-entropy alloys, Elsevier, 2019.

[62] C. Cayron, Quantification of multiple twinning in face centred cubic materials, Acta Materialia 59 (1) (2011) 252–262.

[63] K. V. Thurston, A. Hohenwarter, G. Laplanche, E. P. George, B. Gludovatz, R. O. Ritchie, On the onset of deformation twinning in the crfemnconi high-entropy alloy using a novel tensile specimen geometry, Intermetallics 110 (2019) 106469.